Synthesis, structure and photocatalytic properties of Fe(III)-doped TiO$_2$ prepared from TiCl$_3$

Zoltán Ambrus, Nándor Balázs, Tünde Alapi, Gyula Wittmann, Pál Sipos, András Dombi, Károly Mogyorósi *

Department of Inorganic and Analytical Chemistry, University of Szeged, Research Group of Environmental Chemistry, ReGECh, P.O. Box 440, Szeged H-6701, Hungary

Abstract

Iron(III)-doped titanium dioxide photocatalysts were prepared from aqueous titanium(III) chloride solution in the presence of dissolved FeCl$_3$ (0–10.0 at.% relative to TiCl$_3$) by co-precipitation method. The precipitate was completely oxidized in the aerated suspension, hydrothermally treated, washed and calcinated. The structure of the powders was characterized by thermoanalysis (TG-DTA), diffuse reflectance spectroscopy (DRS), X-ray diffraction (XRD), nitrogen adsorption and transmission electron microscopy (TEM). The light absorption of the iron-containing powders is red shifted relative to the bare sample. The particle size and anatase content were found to significantly decrease at iron contents ≥6.0 at.% which is accompanied with the increase of their specific surface area. XANES measurements showed that the local structure of iron systematically changes with the variation of the dopant concentrations: at higher Fe-contents, hematite- or goethite-like environments were observed, consistent with the formation of separate X-ray amorphous Fe(III)-containing phases. The local structure of iron gradually transformed with decreasing dopant concentrations, possibly due to substitution of Fe(III) in the titania (TiO$_2$) crystal lattice. Energy dispersive X-ray analysis (EDX) and chemical analysis was used to characterize the iron content of the samples in the bulk and X-ray photoelectron spectroscopy (XPS) in the surface layer of the particles. The photocatalytic performance of the prepared photocatalysts was compared with the activity of Aldrich anatase under UV–vis and VIS irradiation in two different photoreactors. Maximum photocatalytic performance was found at 3.0 at.% iron concentration for UV–vis and at 1.2 at.% for VIS irradiation. Doping with iron(III) ions increased the photodegradation rate of phenol by a factor of three for UV–vis irradiation and by a factor of two for VIS irradiation, relative to the bare photocatalyst.

1. Introduction

Since the need for clean environment claims higher standards for the removal of pollutants, the importance of new methods for water and air purification is continuously increasing. Titania (TiO$_2$) as a photocatalyst is widely used for decomposition of toxic organic compounds both in the aqueous and in the gas phase. Generally speaking, titania is efficient for these purification purposes, photostable, environmentally friendly and inexpensive. Many studies have been devoted to synthesize highly active titania photocatalysts with efficiency suitable for practical purposes. However, its large-scale application is still limited because the band gap of photocatalytically more active titania phase (anatase) is 3.2 eV, which requires UV irradiation ($\lambda \leq 387$ nm). The ultimate goal is the direct utilization of solar energy, but the solar spectrum is relatively poor in UV light at the surface on Earth. The other difficulty with TiO$_2$ is the high recombination rate of the photoexcited electron–hole pairs in the irradiated particles. The fast recombination is in competition with the reactions decomposing the pollutants. Many research groups tried to solve these problems by changing the electronic structure of the photocatalyst via doping TiO$_2$ with transition metal ions. Among many candidates, iron(III) ion seems to be the most promising for this purpose. Choi et al. [1] found the highest chloroform degradation efficiency under UV irradiation for a sample containing 0.5 at.% Fe^{3+}. Due to their similar size, the substitution of Ti^{4+} ions in the titania lattice by Fe^{3+}

* Corresponding author. Tel.: +36 62 544 338; fax: +36 62 420 505.
E-mail address: k.mogyorosi@chem.u-szeged.hu (K. Mogyorósi).

ions is favored [1]. The most accepted explanation for the improved photocatalytic performance of iron-doped samples is the generation of shallow charge traps in the crystal structure which decreases the recombination rate of electron–hole pairs. At the same time, the absorption onset of the powders is shifted to the red. Introducing iron ions into the lattice therefore provides photocatalysts not only with lower electron–hole recombination rate but also with excitability by visible light. Enhanced photocatalytic activity was observed for iron-doped photocatalyst under UV [2–9] and also for visible light irradiation in several publications [10–20] both in gas and in liquid phase, for a variety of model compounds (e.g., dye molecules, phenols, oxalic acid, acetaldehyde, acetone, 2-propanol, etc.). An appreciable number of results contradicting those already cited here, have been published in the literature. Some authors observed no or even negative effect of iron on the photocatalytic performance [21–25]. These effects strongly depend on the doping method and the concentration of iron in the photocatalyst. When doping enhanced photoactivity, the optimal concentration of iron was found to be in a very wide concentration range (0.05–20 at.%). Considering, that the different methods may accommodate the iron ions in different positions in the particles, this can well be understood. Colored iron-doped photocatalysts were prepared by several different techniques: incipient wet impregnation method [20,23,25–27], co-precipitation [28–30], sol–gel [1,3,31], flame hydrolysis [32], plasma assisted pyrolysis [10,16,33,34], reactive magnetron sputtering [9,35], mechanical alloying [36], metal organic chemical vapor deposition and metal plasma ion implantation [19,37]. Titanium alkoxides, titanium(IV) chloride and elemental titanium are the most frequently selected precursors for the syntheses in which different iron salts (Fe(NO$_3$)$_3$, FeCl$_2$ and FeCl$_3$) or other iron compounds (Fe(III)Acac, Fe(CO)$_5$ and ferrocene) were employed.

In the present study we report a new co-precipitation technique in which titanium(III) chloride is used. There are two potential advantages of using TiCl$_3$ instead of other conventional Ti-sources. The most obvious is, that TiCl$_3$ solutions are much easier to handle, than the fuming and rapidly hydrolyzing TiCl$_4$ or the viscous and expensive Ti(OR)$_4$. A further advantage is, that the ionic radius of Ti(III) (0.81 Å) is close to that of Fe(III) (0.79 Å), but far from that of Ti(IV) (0.75 Å) [1]. Therefore there is a good chance for isomorphic substitution of Ti(III) (and not Ti(IV)) for Fe(III) during co-precipitation. During the synthesis, the precursor is hydrolyzed and precipitated in the presence of iron(III) ions, by adding aqueous solution of ammonia. The aerated solution containing dissolved oxygen provides the oxidation of Ti^{3+} ions into Ti^{4+} in the process. The sediment is separated, hydrothermally crystallized and finally calcinated. The powders thus obtained were characterized by different techniques and their photocatalytic performance was tested by phenol photodecomposition in water both under UV and VIS irradiation. To the best of our knowledge such preparation method and characterization of iron-doped TiO$_2$ from TiCl$_3$ has not been reported earlier.

2. Experimental

2.1. Materials

Titanium(III) chloride (min. 15 m/m% in HCl solution, containing 5–10% free acid as HCl, Sigma–Aldrich) was used for the synthesis of the titania nanoparticles. The iron(III) was added in the form of FeCl$_3$ × 6H$_2$O (purum, Reanal) to the solution. The pH was adjusted by a concentrated solution of ammonia (28–30%, Sigma–Aldrich). HCl$_{cc}$ (37 m/m%, ACS, Sigma–Aldrich) was used for the synthesis of iron(III)-oxide reference (i.e., Ti-free solid). The chemicals were used as received. In all experiments Milli-Q water was taken as aqueous media. Phenol (99.8%, Sigma–Aldrich) was selected for the photocatalytic tests, its decomposition was monitored by HPLC analysis. Titanium dioxide powders (anatase and rutile, 99.9%, Sigma–Aldrich) were used as X-ray diffraction (XRD) calibration and photocatalytic standards. Rutile standard was heated before use at 1000 °C for 1 h in order to convert anatase traces completely to rutile. Zinc oxide (Reanal, 99%) was used as an internal standard for the determination of the crystal phase composition of the photocatalysts.

2.2. Synthesis of the photocatalysts

The non-doped titania photocatalyst was prepared by using the recipe described by Di Paola et al. [25]. 100 mL of the Ti(III) chloride solution was placed into a flask. Aqueous solution of a concentrated ammonia solution (80 mL) and distilled water (50 mL) were mixed and then added dropwise to the titanium precursor solution in about 10 min under vigorous magnetic stirring at room temperature. Introducing the first droplets, precipitation was immediately observed in the dark bluish-purple solution. The suspension thus obtained contained dark blue precipitate. The stirring was continued at room temperature for 16 h, during which the color of the dispersion gradually turned to white. The final pH of the dispersion was found to be ∼8.5. The suspension (ca. 150 mL) was loaded in a PTFE coated steel container (inner volume is ca. 190 mL) equipped with a screw cap. The autoclave was placed in a hot box oven for 24 h at 110 °C. Subsequent to the hydrothermal heat treatment, the samples were washed with distilled water and centrifuged several times in order to remove the NH$_4$Cl side product. The purified sediment was then dried at 80 °C for ≥10 h. The powder was ground and placed into a quartz boat and calcinated in a tubular furnace under air flow at 500 °C for 4 h (the heating rate applied was 10 °C/min). The powder was allowed to cool in the air flow at a natural cooling rate and then re-pulverized. A post-calcination was carried out for one more hour under the same conditions.

The iron(III)-doped photocatalysts were prepared in a procedure identical to that of the bare catalyst, except that the calculated amount of solid FeCl$_3$ × 6H$_2$O was dissolved in the titanium(III) chloride solution before the addition of the ammonia solution. Samples with different iron contents were prepared such as 0.1, 0.6, 1.2, 3.0, 6.0 and 10.0 at.% (determined as $n_{Fe}/(n_{Fe} + n_{Ti}) \times 100$). The samples are denoted

by acronyms which indicate their added iron content in at.%, for example: TiO$_2$–1.2Fe.

2.3. Characterization of the photocatalysts

Formation of the nanocrystals was studied by thermo-analytical measurements using a MOM Derivatograph Q-1500 D instrument. The necessary calcination temperature for anatase formation was determined from the TG and DTA curves (see below).

Ocean Optics diode array spectrophotometer was used to record the UV–vis spectra of the photoreactor lamps. A Mikropack NanoCalc 2000 diode array spectrophotometer was used with an integration sphere (ISP-50-8-R-GT) and Lab-sphere (WS-1-SL) white reflection standard with Spectralon for measuring the DR spectra of the powders (λ = 330–800 nm).

XRD experiments were carried out in a Philips X-ray diffractometer (PW 1930 generator, PW 1820 goniometer) with Cu Kα radiation (λ = 0.15418 nm) at 2Θ = 20–40°. The average diameters of the TiO$_2$ particles (D_{TiO_2}) were obtained by means of the Scherrer equation [$D = k\alpha/\beta \cos \Theta$, where β = line broadening ($\beta = \beta_s - \beta_0$, where β_s and β_0 are the half-widths of the XRD peaks of the sample and of the silicon standard), k the related to the crystallite shape (k = 0.9), and α and Θ are the radiation wavelength and Bragg angle, respectively]. A single-crystal silicon standard ($\beta_0 = 0.105°$ (2Θ)) was used for calibration. In order to characterize the phase composition of the powders, calibration curves of the anatase and rutile phases were determined. Mixtures of rutile and anatase standards were prepared at different ratios, i.e., 0–100, 20–80, 40–60, 60–40, 80–20 and 100–0 wt%. These individual mixtures of crystalline titania standards were mixed with a ZnO internal calibration standard in a 80–20 wt% ratio. The diffraction peaks recorded were integrated and their area values were always normalized to the averaged area of the ZnO standard peaks (100 reflection) in the calibration. This way the uncertainties caused by any systematic or random variations in the instrumental parameters were minimized.

To determine particle size and morphology, transmission electron microscopy (TEM) images were obtained on a Philips CM-10 electron microscope, using an accelerating voltage of 100 kV. The powders were suspended in water, dropped on copper grids (diameter 3 mm) covered by Formwar foil and dried at room temperature.

Specific surface areas of photocatalysts were determined by a Micromeritics gas adsorption analyzer (Gemini Type 2375) at 77 ± 0.5 K in liquid nitrogen. Prior to measurements the samples were pretreated in a vacuum at 100 °C for 12 h. The sample vessel was loaded with ca. 0.15–0.25 g of samples. The adsorption isotherms were analyzed by means of the BET equation.

To determine the local structure of Fe(III) in the TiO$_2$ matrix, XANES spectra of three representative iron-doped samples were recorded. XANES measurements at the Fe K-edge were performed on beamline I811 at Maxlab, Lund, Sweden. Measurements were recorded in the fluorescence mode.

SEM-EDX analysis was performed on a Hitachi S-4700 scanning electron microscope equipped with a Röntec QX2 EDS unit operating at 20 kV and 12 mm working distance.

XP spectra were taken with a SPECS instrument equipped with a PHOIBOS 150 MCD 9 hemispherical electron energy analyzer operated in the FAT mode. The excitation source was the Kα radiation of a magnesium anode ($h\nu$ = 1253.6 eV). The X-ray gun was operated at 180 W power (12 kV, 15 mA). The pass energy was set to 20 eV, the step size was 25 meV, and the collection time in one channel was 150 ms.

Atomic absorption spectrometry was used to determine the iron content in the powders after dissolving them in HF-H$_2$SO$_4$ solution.

2.4. Determination of the photocatalytic activities

In our experiments, two different photoreactors were used, one of them is suitable for UV irradiation experiments (Photoreactor A) and the other one for visible light (VIS, $\lambda > 400$ nm, Photoreactor B) irradiation experiments. 1 g L^{-1} photocatalyst addition was used throughout the experiments. The photocatalyst powder was dispersed in a phenol-containing aqueous solution. Permanent air bubbling was applied during irradiation in order to keep the concentration of the dissolved oxygen constant. Photoreactor A was an open Pyrex glass tube with double walls, surrounded by a thermostating jacket at 25.0 ± 0.2 °C, into which 100 mL of the suspension to be studied was poured. The tube reactor was surrounded and irradiated by six fluorescent lamps (Vilber-Lourmat T-6L UV-A, 6W power, radiation maximum at 365 nm) providing a radiation intensity of $I_A = 1.02 \pm 0.01 \times 10^{-5}$ Einstein dm^{-3} s^{-1} (λ = 320–500 nm) determined by chemical actinometry.

Photoreactor B was an immersion type HERAEUS Labor-UV-Reactorsystem 1 equipped with an OSRAM metal halide lamp (Power Star HCl-TC 35 W/WDL type). The spectrum of the lamp was slightly modified by circulating NaNO$_2$ solution (1 M) in the thermostating jacket. This solution absorbs photons of $\lambda \leq 400$ nm, providing visible light irradiation for the samples ($I_B = 7.6 \pm 0.1 \times 10^{-6}$ Einstein dm^{-3} s^{-1} at λ = 400–500 nm).

Samples (2 mL) were taken from the suspensions at certain irradiation times, centrifuged and filtered through 0.02 μm Anotop filters. Under the experimental conditions employed, the direct photolysis of phenol has been checked and was found to be insignificant. There was no observable change in the phenol concentration of the suspension in dark for 3 h under air bubbling. Before turning the lamps on, 10–15 min time was allowed the system to get homogenized. This is expected to be sufficient, as the photocatalysts prepared are non-porous.

The concentration of phenol in the filtrate was determined by using HPLC. The analytical instrument was an Agilent 1100 series LC system consisting of a binary pump, a micro vacuum degasser, a diode array detector (λ_d = 210 nm), a thermostated column compartment and ChemStation data managing software. The chromatographic system was equipped with Rheodyne Model 7725 injector with a 20 μL loop and a ZORBAX Eclipse XDB-C8 column (4.6 mm × 150 mm). The

eluent consisted of a 10:18 methanol:water (v/v) mixture, and the flow rate was 0.8 mL min^{-1}. The concentration data of phenol in the filtrate were plotted versus the irradiation time. The initial degradation rate was calculated from the fitted decay curves.

3. Results and discussion

3.1. Characterization of the photocatalysts

The photocatalysts were prepared from the hydrolysis of titanium(III) chloride in aerated suspensions at about pH 8.5. As the pH of the solution increased by adding ammonia, immediate precipitation of Ti(OH)$_3$ occurred. The suspension contained dark bluish precipitate which later slowly became light blue and finally white indicating the oxidation of titanium(III) to titanium(IV) by atmospheric oxygen. In the presence of iron(III) ions co-precipitation of Fe(III)-oxide–hydroxide took place. The titanium(IV)–iron(III)-oxide–hydroxide mixtures resulted from the syntheses described in the experimental part are amorphous, therefore various heat treatments are necessary for obtaining photocatalytically active (i.e., crystalline) titania. First, hydrothermal heat treatment was used at 110 °C for 24 h. To make crystallization complete, the hydrothermally treated powders are needed to be further crystallized at elevated temperatures. To determine the optimal calcination temperature, thermoanalytical measurements were employed. The weight loss of the bare hydrothermally treated titanium(IV)-oxide–hydroxide is completed at about 500 °C (at a heating rate of 10 °C/min, see Fig. 1). The approximately 9.5 wt% loss can be attributed to a multistep polycondensation process of titanium(IV)-oxide–hydroxide. DTA measurements established that the transformation of TiO$_x$(OH)$_y$ into TiO$_2$ involved the endothermic loss of water from 50 to 300 °C with a peak at 150 °C. This was followed with an exothermic peak (between 300 and 560 °C, its maximum is at about 460 °C) which is attributed to the formation of anatase from amorphous TiO$_2$. Anatase is finally transformed at 770–870 °C to rutile in

an exothermic process. The exotherm peak of anatase formation was shifted to lower temperatures at increasing iron content. The original exotherm peak was found for bare TiO$_2$ at 457 °C, which was shifted to 454 °C for TiO$_2$–1.2Fe and to 419 °C for TiO$_2$–10.0Fe sample. From the DTA curves, the most important information is that the crystallization of anatase is expected to occur around 460 °C. However, to avoid sintering of the nanoparticles (i.e., loss of active surfaces) as well as the formation of rutile, temperatures much higher than 460 °C should be avoided. Therefore, for the calcination of the samples 500 °C was selected.

The DR spectra of the powders prepared are shown in Fig. 2. For comparison, the spectrum of Aldrich anatase is also shown. The spectrum of bare TiO$_2$ clearly shows an absorption onset at about 395 nm which is in good agreement with the band gap value of bulk anatase ($\lambda = 387$ nm corresponding to 3.2 eV).

The DR spectra are systematically red shifted as the added iron content increases. This can also be concluded from a simple visual inspection of the samples since their color gradually turns from white to brownish-red. This means that the samples can absorb light in a quite broad spectral range (up to $\lambda = 600$ nm) in the visible region of the spectrum which is a prerequisite for the utilization of the visible light for photocatalysis.

The phase composition of the samples was determined by X-ray diffraction technique. Fig. 3 shows the diffraction patterns of the calibration mixtures prepared according to the method described in the experimental part. For the analysis, three peaks were fitted and integrated for each pattern: the main reflection of anatase ((1 0 1), at 25.3° (2Θ)), rutile ((1 1 0), at 27.5° (2Θ)) and zinc oxide ((1 0 0), at 31.8° (2Θ)). The area values of ZnO were averaged for the six-calibration pattern, and then each ZnO peak area value of the given pattern was normalized to that averaged value (this gave a normalization factor for each pattern). The anatase and rutile peak area values were corrected by that given factor. The corrected area values were plotted versus the anatase and rutile content determining the two calibration curves. To analyze an unknown sample, we need to
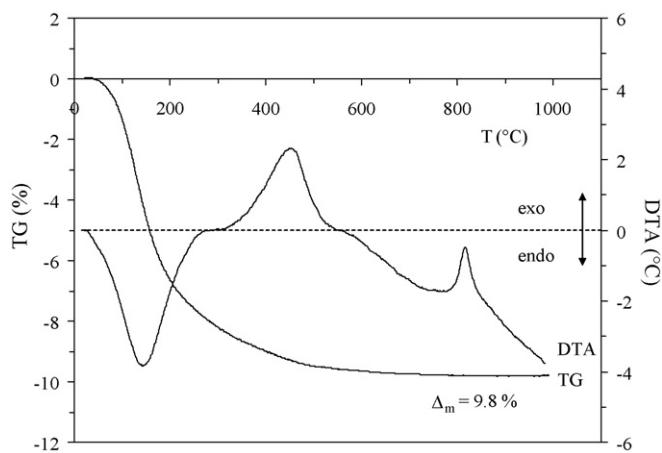

Fig. 1. Thermoanalytical curves (TG and DTA) of hydrothermally treated titanium(IV)-oxide–hydroxide sample determined in still air at a heating rate of 10 °C/min.
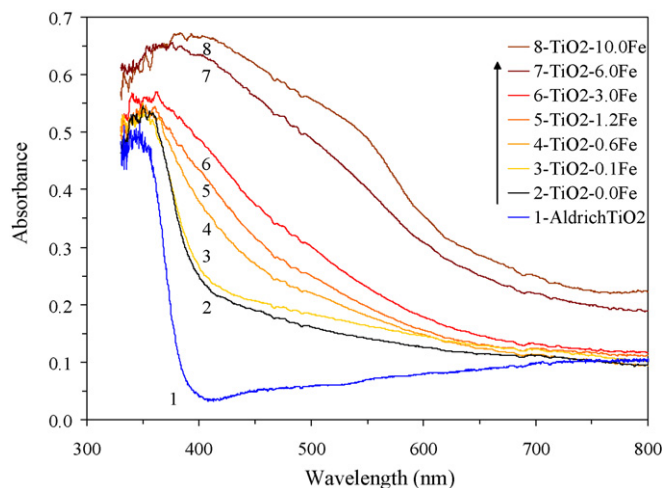

Fig. 2. Diffuse reflectance spectra of Aldrich anatase, and the bare and iron-doped TiO$_2$ samples (Fe-contents: 0.0, 0.1, 0.6, 1.2, 3.0, 6.0 and 10.0 at.%).
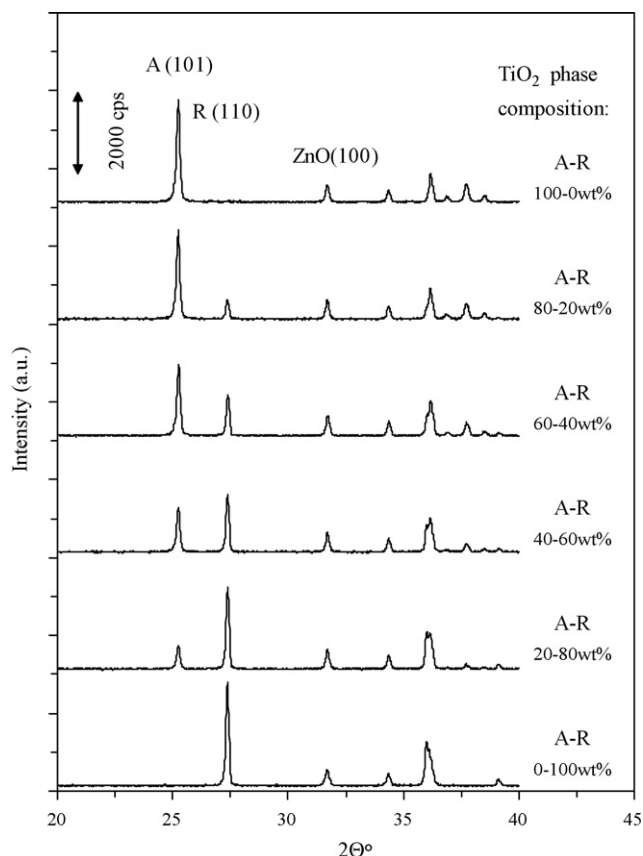
Fig. 3. X-ray diffraction patterns for the determination of the calibration curves of crystalline titania phases, such as anatase and rutile using ZnO internal standard (20 wt%).

Fig. 4. XRD patterns of bare TiO_2 and iron-doped titania (1.2 and 10.0 at.%) samples. XRD pattern of α-Fe_2O_3 (hematite) prepared under titanium-free conditions is also shown (uppermost pattern) A and B stand for anatase and brookite, respectively.

do the same normalization for its peaks and then the anatase and rutile phase content can directly be determined from the calibration curves. Our results confirmed the assumption that using an internal standard for this calibration significantly enhances reproducibility. It was found, that this method eliminates uncertainties associated with variations (both random and systematic) in the experimental conditions, especially in the preparation of the powder layer in the sample holder (for example in its compactness).

The XRD pattern of the iron-doped samples is shown in Fig. 4. The calcinated samples were found to contain anatase only. Trace amount of brookite was found in bare TiO_2 (at $2\Theta = 30.8°$, marked by B in Fig. 4). Titanium(III) chloride was used earlier by other groups for preparing titanium dioxide [25,38–41]. Depending on the conditions, especially on the applied pH of the precipitation, different titania phases or their mixtures were produced. Our observations are in agreement with those of Cassaignon et al. [39], who studied the effect of pH of the medium at 60 °C and found that mainly brookite can be produced under the most acidic condition (1 < pH < 2.5), when rutile is formed in the less acidic condition (pH 2.5–4.5) and anatase with some brookite can be synthesized at pH > 4.5. They also described the oxidation of the dark solid precipitate as a very fast process at pH > 4.5 which results in an amorphous titanium dioxide. In our experiments, adding ammonia solution into the strongly acidic titanium(III) chloride
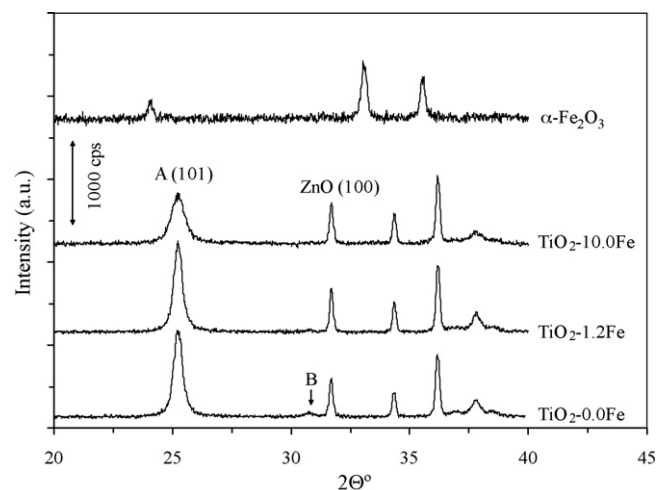
solution, rapidly increased the local pH at the place of dropping. This was obviously beneficial for the formation of a titanium(III)-oxide–hydroxide precipitate which then was relatively quickly oxidized by the dissolved molecular oxygen. Significant bleaching of the dark blue colored precipitate occurred in the first 30 min. The final pH of the suspension was about 8.5, hence rutile phase was not formed.

Iron(III) oxide was synthesized in the same process described in Section 2.2 in Ti(III) free systems (upper pattern in Fig. 4) resulting in Fe_2O_3 powder in the hematite crystal phase (α-Fe_2O_3) [30]. Clearly, these diffraction peaks are completely missing from the diffraction patterns of the iron-doped powders. Note, that the low sensitivity of the XRD method might prevent from observing the separate Fe_2O_3 phase in these samples, due to the low concentration of added iron. However, even in the case of the sample with 10.0 at.% iron, presence of hematite is not observed. The lack of separate iron-oxide phase can likely be interpreted either by the incorporation of iron(III)-ions in the anatase crystal structure substituting Ti(IV) ions, or by very fine dispersion of hematite in the titania resulting in X-ray amorphous behavior.

The anatase content was found to be approximately 96–99 wt% for the samples containing iron ≤1.2 at.% (Fig. 5). Samples with similar iron content prepared by flame aerosol synthesis [18,32–34] were found to be constructed from significant amounts of rutile, which is a direct consequence of the higher temperature applied there. This means that using the sol–gel method followed by calcination at lower temperatures (<550 °C), provides more freedom to vary the iron content in wider concentration range and with the ability of reserving the anatase crystal form.

As the iron content was further increased (from 1.2 to 10.0 at.%), the anatase content gradually decreased to 73 wt%. The decrease in the anatase content, since no other crystalline phase (e.g., rutile) was detected, should mean that the sample contains some X-ray amorphous titanium(IV)–iron(III) oxide.
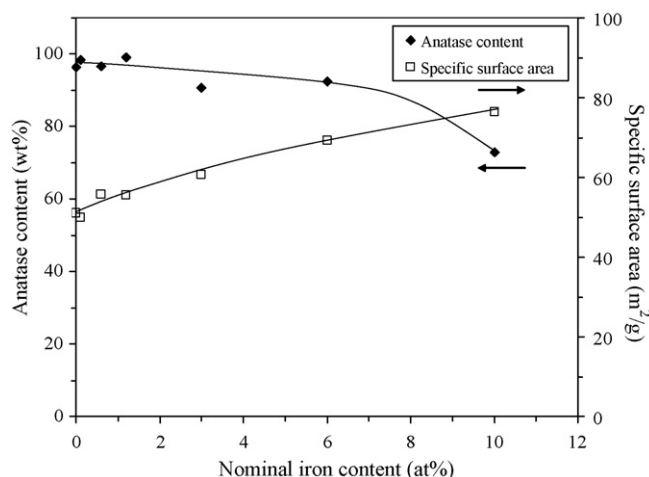
Fig. 5. The anatase content and specific surface area values of the powders prepared.

(For this, it had to be assumed, that peak intensities are not significantly distorted by crystal size effects. Given, that in our systems particle diameters are always >14 nm, this assumption is reasonable.) At the same time the particle size of anatase calculated from the line broadening follows a similar trend. The diameter of the nanoparticles is about 23–25 nm for the samples at 0–1.2 at.% iron content, further increasing the iron concentration the particle diameter gradually decreases to 15 nm. Specific surface area of the samples increases with the increasing iron content from 50 to 76 m^2/g which is due to the smaller particles and the possible presence of amorphous materials. Similar trend was found by Teoh et al. [18]. These observations are also confirmed by TEM studies. Since the particles are non-spherical, many of them are somewhat elongated, their diameter was calculated via measuring the area of each particle and then calculated an equivalent diameter of a circle with the same area. The TEM image of bare TiO_2 (Fig. 6a) contained nanoparticles in the particle diameter range of 13–48 nm ($D_{av} = 30$ nm). The size distribution of this polydisperse sample cannot be precisely determined from these images since the strong aggregation of the particles on the grid. Similar sizes are found on the sample containing 1.2 at.% iron (Fig. 6b, $D = 14$–49 nm, $D_{av} = 28$ nm). The third TEM image (Fig. 6c) reveals that the nanoparticles were formed indeed with smaller sizes ($D = 7$–29 nm, $D_{av} = 16$ nm) when 10.0 at.% iron was added during the synthesis. The particle diameters determined from XRD line broadening (23.9, 23.7 and 14.6 nm, respectively) are somewhat smaller than those estimated from the presented TEM images.

Fig. 7 shows the fluorescent XANES spectra of the samples with 0.6, 3.0 and 10.0 at.% iron content, respectively. The differences between these spectra are subtle, but significant and indicate systematic variations in the local structure of iron in the samples studied. Comparison of these spectra made it possible to qualitatively assess the local structure around the Fe(III). With the decreasing iron-content, the main peak at ca. 7130 keV gradually sharpens and the shoulder around 7140 keV (which is a characteristic feature in the XANES spectrum of various forms of Fe(III)-oxides and oxy-hydro-

xides [42]) gradually decreases. The spectrum obtained at the highest Fe(III)-concentration is reminiscent to the XANES spectrum of α-Fe$_2$O$_3$ (hematite) and α-FeOOH (goethite) [42]. On this basis, the iron is most likely to be present in this sample as separate X-ray amorphous phase (hematite or goethite) physically mixed with the TiO_2. The nature of the incorporated iron at lower concentrations is significantly different from that of the hematite- or goethite-like structures, and is most likely to be substitutional. Similar observations were very recently described for iron-doped TiO_2 samples in the literature [43,44], but further measurements (i.e., determination and evaluation of the EXAFS spectra of these samples) are needed to confirm this statement regarding our own samples. Such measurements are currently in progress.

Energy dispersive X-ray analysis (EDX) was carried out on the TiO_2–1.2Fe, TiO_2–3.0Fe and TiO_2–10.0Fe samples in order to determine the average (bulk) iron content. The spectra clearly indicated the presence of iron, the $n_{Ti}/(n_{Ti} + n_{Fe})$ atomic ratio was found to be 1.29, 3.3 and 10.4 at.%, respectively. This is in good agreement with our nominal iron concentrations in the samples. Since EDX is considered to be a semi-quantitative analytical method, we did chemical analysis on our samples as well. The iron content of the samples were analyzed by atomic absorption spectrometry. Data are represented in Table 1. The iron content of the bare TiO_2 was relatively high which is most likely originated from the $TiCl_3$ solution used in the synthesis. The samples with higher iron content had a loss of iron in about 20–25%. We can assume that the smallest nanoparticles were rich in iron and a certain amount was washed away during the centrifugation-washing process after the hydrothermal heat treatment (before calcination). A further uncertainty might arise from the error in the nominal Ti^{3+} content of the stock solution (which was stated to be min. 15%).

In order to elucidate the nature of incorporation of iron in the samples, the anatase peaks at 25.3° and 48.1° (2Θ) were used for calculating the unit cell parameters. We experienced some difficulties with the reproducibility of the exact peak positions therefore we used ZnO internal standard for making the characterization more precise (the powders contained 20 wt% ZnO). The position of ZnO reflection (1 0 0) provides a good calibration tool for the 2Θ scale of the patterns (the largest correction was +0.06° (2Θ)). Applying this method no significant difference in the position of the 1 0 1 anatase reflection was found (25.30–25.32°) comparing the bare and

Table 1
Iron content of the samples determined from chemical analysis

Catalyst	Nominal iron content (at.%)	Iron content from AAS (at.%)
TiO_2–0.0Fe	0.0	0.182
TiO_2–0.1Fe	0.1	0.261
TiO_2–0.6Fe	0.6	0.670
TiO_2–1.2Fe	1.2	0.886
TiO_2–3.0Fe	3.0	2.240
TiO_2–6.0Fe	6.0	4.722
TiO_2–10.0Fe	10.0	7.873
TiO_2 Aldrich	–	–
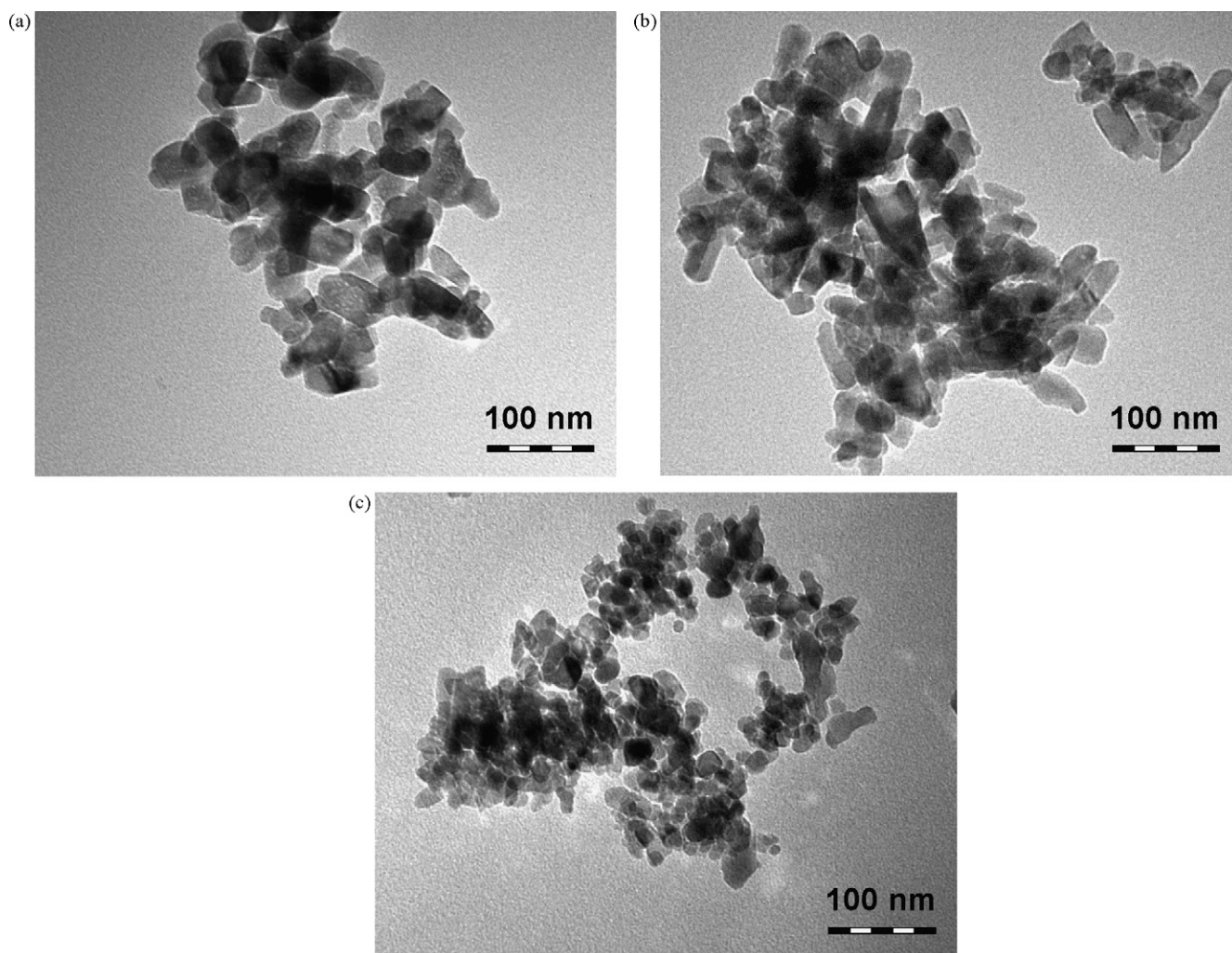
Fig. 6. Representative TEM images of the (a) bare TiO_2, (b) TiO_2–1.2Fe and (c) TiO_2–10.0Fe samples.

iron-doped titanias. XRD data in the literature show ambiguous results indicating opposite trends (shift to lower [7,28,34] or higher [11,17,30] 2Θ angles) or very small effects which might be also associated with experimental errors. There are many papers in the literature describing iron-doped TiO_2 samples without any observed change in the positions of the XRD peaks measured [4–6,8,10,13–15,19,21,22,29,32]. Although many authors explained certain properties with the substitution of Ti^{4+} by Fe^{3+}-ions, they did not report such changes in the lattice parameters from their XRD data. It is possible that the small difference in the size of Fe^{3+} and Ti^{4+} ion results in hardly detectable differences in the XRD peak positions. The improved activity of the iron-doped photocatalyst might also come from the iron-containing surface of titanias or a nanocomposite structure, which would not show up in terms of any shifts in the XRD peak positions.

X-ray photoelectron spectroscopy (XPS) was also used to reveal the state of iron in the samples. This technique is suitable for determining the titanium–iron ratio in the samples in the top 1–2 nm layer of the particles. Two samples were investigated: TiO_2–1.2Fe and TiO_2–10.0Fe. The presence of Fe^{3+} in the

Fig. 7. XANES spectra of the TiO_2–0.6Fe, TiO_2–3.0Fe and TiO_2–10.0Fe samples.

samples is clearly indicated by the peak found at 710.9 eV (Fe $2p_{3/2}$) and at 724.4 eV (Fe $2p_{1/2}$). The satellite peak at 719.0 eV also confirms the presence of Fe^{3+}. Titanium peaks were found at 458.7 eV (Ti $2p_{3/2}$) and 464.3 eV (Ti $2p_{1/2}$) which belong to Ti^{4+}. The presence of Ti^{3+} cannot be confirmed from these experiments. The results show 8.4 and 18.8 at.% iron content ($n_{Fe}/(n_{Fe} + n_{Ti})$) for the TiO$_2$–1.2Fe and TiO$_2$–10.0Fe samples, respectively. The higher surface concentration of iron indicates that during the synthesis a certain amount of dopant is accumulated in the surface layer.

3.2. Photocatalytic performance of the samples

The photocatalytic activities of the samples were determined under UV–vis irradiation (Photoreactor A) and VIS only irradiation (see details in Section 2.4). The irradiation spectra are shown for the two types of photoreactors in Fig. 8. As it can be seen on the spectrum of Photoreactor B, there is no UV light transmitted to the suspension through the cooling jacket containing NaNO$_2$ solution. Phenol decomposition was followed in aqueous suspension of the samples prepared. The initial concentration of phenol was chosen to be 0.5 mM for the suspensions irradiated under UV–vis and 0.1 mM for the VIS irradiation experiments, since the decomposition rate was much lower in the latter case. For the same reason, 120 min irradiation time was selected for the UV–vis irradiation experiments and 180 min for the VIS irradiation experiments. There was not any detectable decrease in the concentration of phenol under the same conditions without photocatalyst. By using these parameters, the decay curves (see Fig. 9a and b) can be used for the determination of the initial decomposition rate of phenol for the different photocatalysts. The decay curves were fitted with an empirical function and the initial reaction rate (r_0) was calculated from their slope at $t = 0$ time.

The decomposition of phenol was accelerated in the presence of iron in the photocatalyst to a certain Fe-concentration in both reactors. All the structural parameters of the photocatalysts and the initial reaction rate data are
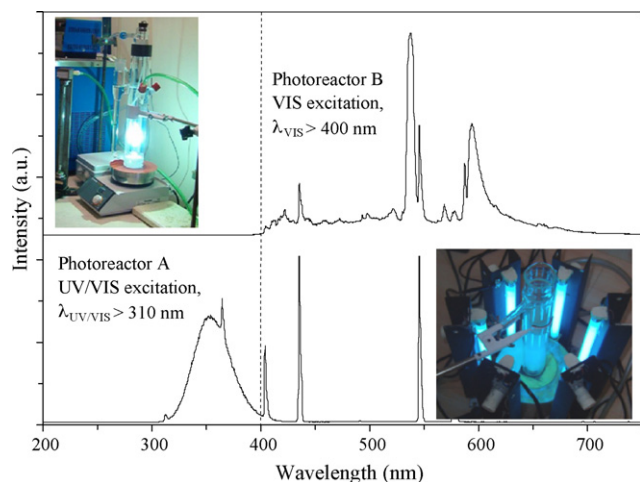

Fig. 9. Photodecomposition curves of phenol under UV–vis (a) and VIS (b) irradiation for photocatalysts with different iron content ($c_{0,UV-vis} = 0.5$ mM, $c_{0,VIS} = 0.1$ mM; 1.0 g/L photocatalyst, detection at $\lambda = 210$ nm).

Fig. 8. The irradiation spectra in the UV–vis ($\lambda > 310$ nm) and VIS ($\lambda > 400$ nm) experiments. Photos of the Photoreactors A and B are also shown.
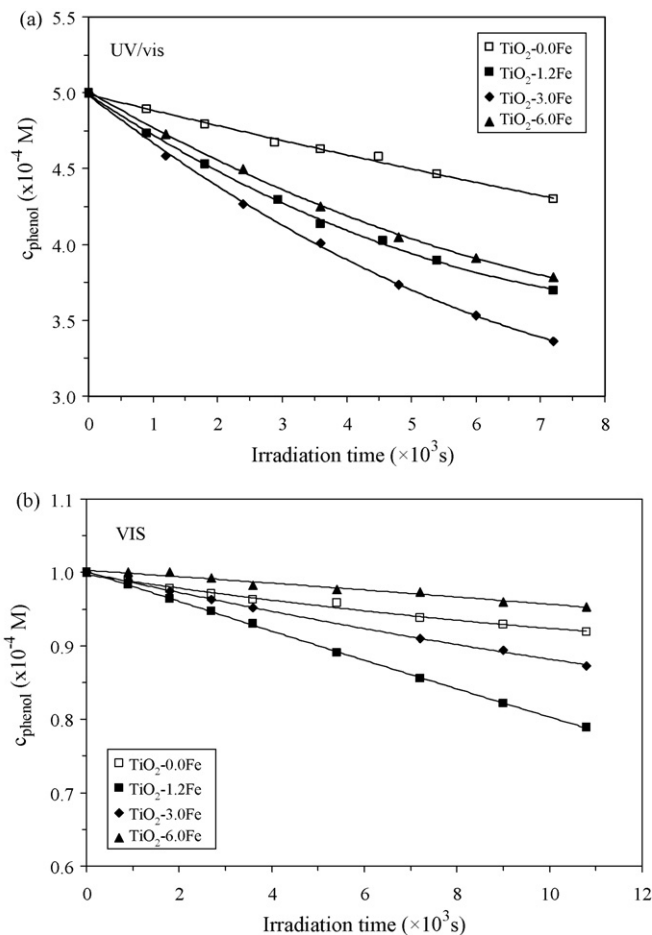
summarized in Table 2. Comparing the undoped TiO$_2$ with the Aldrich anatase, which is one of the best commercially available photocatalysts, we can see that our sample has relatively low activity under UV–VIS irradiation. On the basis of literature data, TiO$_2$ samples with specific surface area much larger than that of commercial photocatalysts (e.g., Degussa P25 or Aldrich anatase) can readily be prepared by a variety of sol–gel methods followed by calcination. However, in the waste majority of the cases, the photocatalytic performance of these catalysts is far below that of P25 or Aldrich anatase. It seems that there is no direct univariate correspondence between the photocatalytic performance and specific surface area. Other parameters, like surface hydrophilicity, surface oxygen adsorption capacity, etc. also play crucial role in determining the photocatalytic performances. The crystallization of the photocatalyst requires higher temperatures, but this is accompanied with the loss of surface hydrophilicity. The dehydroxylated surface of the particles causes higher aggregation in the aqueous suspension which is obviously detrimental to the photocatalytic activity as many particles are hidden for the light absorption. Introducing iron into the crystal structure may also improve the wettability of the nanoparticles [45]. The highest initial decomposition rate of phenol was found to be at

Table 2
Structural parameters and initial photodecomposition rates of phenol under UV–vis and VIS irradiation for the prepared titania samples with different iron content and for Aldrich anatase (estimated uncertainties: a_{BET}^S : ±5%; particle diameter: ±10%; anatase content: ±5%; r_0: ±10%)

Catalyst	Nominal iron content (at.%)	a_{BET}^S (m²/g)	D_{an} XRD (nm)	Anatase content (wt%)	Reactor A, $r_{0,UV-vis}$ (×10⁻⁸ M s⁻¹)	Reactor B, $r_{0,VIS}$ (×10⁻⁸ M s⁻¹)
TiO₂–0.0Fe	0.0	51.0	23.9	96.4	1.05	0.095
TiO₂–0.1Fe	0.1	50.0	25.1	98.4	1.06	0.089
TiO₂–0.6Fe	0.6	55.7	22.7	96.6	1.21	0.124
TiO₂–1.2Fe	1.2	55.5	23.7	99.1	2.71	0.207
TiO₂–3.0Fe	3.0	60.6	20.0	90.8	3.29	0.142
TiO₂–6.0Fe	6.0	69.2	17.8	92.5	2.47	0.042
TiO₂–10.0Fe	10.0	76.3	14.6	73.0	1.49	0.043
TiO₂ Aldrich	–	<10	>100	100	8.27	0.072

the 3.0 at.% iron content for UV–vis irradiation and at 1.2 at.% for VIS irradiation. Similar (1–3 at.%) optimum iron content was found by Adán et al. [7], Wang et al. [16] and Carneiro et al. [35]. However, it should be noted that a very wide range of optimum iron content can be found in the literature (0.05–20 at.%). Its optimal value might depend on a variety of parameters, such as the synthesis method and conditions, and also on the substrate itself. Zhang et al. [4] found a very interesting correlation between the optimum iron content and the size of the photocatalyst particles. They found that larger nanoparticles require lower iron concentration to reach their maximum photocatalytic activity. The nanoparticles prepared by us are relatively large, therefore they are expected to reach the optimum photoactivity around 0.05 at.% iron content on the basis of [4]. However, Zhang et al. observation is probably not generally true due to the very complex nature of heterogeneous photocatalysis.

The dual role of iron in the photocatalytic processes was described [6,8,14] such as electron (Eqs. (1) and (2)) and hole trap (Eqs. (3) and (4)):

$$Fe^{3+} + e^- \rightarrow Fe^{2+} \tag{1}$$

$$Fe^{2+} + O_{2(ads)} \rightarrow Fe^{3+} + O_2^{\bullet -} \tag{2}$$

$$Fe^{3+} + h_{vb}^+ \rightarrow Fe^{4+} \tag{3}$$

$$Fe^{4+} + OH^- \rightarrow Fe^{3+} + OH^{\bullet} \tag{4}$$

Since iron(III) ions can act as electron and hole trap and they can release both charge carriers to the solution phase (Eqs. (2) and (4)) or directly to the substrate, the recombination rate of the electron–hole pairs is lowered, therefore the photocatalytic activity is enhanced. It should be noted, however, that at higher iron concentration the iron(III) ions may act as recombination centres as well [14]:

$$Fe^{3+} + e^- \rightarrow Fe^{2+} \tag{5}$$

$$Fe^{2+} + h_{vb}^+ \rightarrow Fe^{3+} \tag{6}$$

Since a competition exists among these redox processes, a certain amount of iron(III) ion can work with the best efficiency.

The enhancement of the photocatalytic activity of bare TiO₂ can be illustrated by calculating the ratio of the initial decomposition rate of phenol for iron-doped photocatalyst and r_0 determined for bare TiO₂ ($r'_{0,phenol}$, see Fig. 10). The initial photodecomposition rate was enhanced approximately by a factor of three for UV–vis irradiation and by a factor of two for VIS irradiation. One would expect the enhancement for VIS irradiation to be higher, considering, that bare TiO₂ should not be active at these excitation wavelengths at all. For example the ratio of the $r_{0,UV-vis}/r_{0,VIS}$ for Aldrich anatase is ∼115, but the same number for bare TiO₂ prepared from TiCl₃ is ∼11. From the DR spectra of the powders (Fig. 2), one can see that Aldrich anatase has no appreciable absorption at λ > 390 nm. However, for the TiO₂–0.0Fe sample this is not the case, it has some absorption between 400 and 600 nm. This means, that the TiO₂–0.0Fe sample can be excited by visible light to a certain extent. This unexpected observation is most likely caused by the presence of nitrogen (as ammonia) in the synthesis, as synthesis repeated by using NaOH instead of NH₄OH resulted in almost completely inactive powder ($r_0 = 0.005 \times 10^{-8}$ M s⁻¹). Although the samples were washed several times before drying and calcination, it is still possible that some nitrogen remained in the hydrolyzed amorphous titania, which finally resulted in a little nitrogen doping of bare TiO₂. Nitrogen-doped titania from TiCl₃ was prepared by a couple of research groups [46–48] using
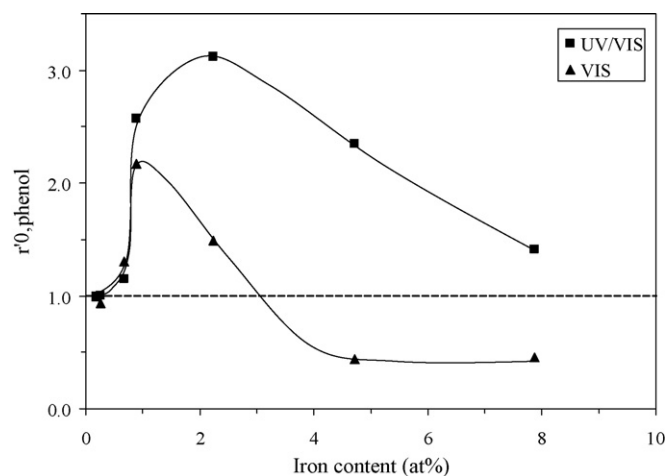

Fig. 10. Photocatalytic enhancement of the iron-doped titania samples for the photodecomposition of phenol under UV-vis and visible light irradiation.

different nitrogen sources (urea, hydroxylamine and hexamethylenetetramine) in solvothermal treatments. The presence of doping nitrogen expanded the excitability into the visible domain of the spectrum and caused also some enhancement of these samples. XPS experiments confirmed a trace amount of nitrogen on the surface (peak found at 400 eV). Although our samples may contain a small amount of nitrogen, the main photocatalytic enhancement is achieved because of the presence of iron(III) ions incorporated in the anatase crystal lattice.

4. Conclusions

Iron-doped titanium dioxide can be readily prepared by a co-precipitation method using acidic solutions of $TiCl_3$ and $FeCl_3$. Increasing the pH of the medium by slow addition of aqueous ammonia solution resulted in the co-precipitation of the metal ions. The iron(III)–titanium(III)-oxide–hydroxide precipitate was then oxidized by the dissolved atmospheric oxygen. After hydrothermal treatment and calcination, colored anatase photocatalysts with different iron content were synthesized—as the XRD and diffuse reflectance spectroscopy (DRS) investigations confirmed. The anatase content was about 96–99 wt% for the samples with lower iron content (0–1.2 at.%). Further increase in the iron content (up to 10.0 at.%) increases the amount of X-ray amorphous phase (27 wt%), but no crystalline iron(III)-oxide phase was observed. The particle diameter decreases (from 25 to 15 nm) while the specific surface area increases (from 50 to 76 m^2/g) with the increasing iron content. XANES studies revealed that at high-dopant concentrations the local environment of iron(III) ions is similar to that of hematite or goethite, but at low iron concentrations incorporation of iron in the crystal lattice might take place. XRD data did not unambiguously confirm any deformation of the anatase crystal structure, although the substitution of Ti^{4+} by Fe^{3+} cannot be excluded. The improved activity of the iron-doped photocatalyst might also be associated with the iron-containing surface of titanias or a nanocomposite structure, which would not show up as shifts in the XRD peak positions.

Some loss of iron during the synthesis was confirmed by chemical analysis. The iron concentration of the surface layer was higher than the bulk concentration determined by XPS.

The photocatalytic efficiency of iron-doped titanias was found to be superior to the bare TiO_2 under UV–vis irradiation. The photocatalyst with 3.0 at.% iron was the most efficient for the photocatalytic decomposition of phenol in UV–vis experiments. The optimal iron content was found to be 1.2 at.% for VIS light irradiation. At higher iron contents (6.0–10.0 at.%) the photocatalytic performance under VIS irradiation was worse relative to the undoped TiO_2.

Acknowledgements

References

[1] W. Choi, A. Termin, M.R. Hoffmann, J. Phys. Chem. 98 (1994) 13669.
[2] C. Wang, D.W. Bahnemann, J.K. Dohrmann, Chem. Commun. (2000) 1539.
[3] C. Wang, R. Pagel, J.K. Dohrmann, D.W. Bahnemann, C. R. Chim. 9 (2006) 761.
[4] Z. Zhang, C.-C. Wang, R. Zakaria, J.Y. Ying, J. Phys. Chem. B 102 (1998) 10871.
[5] M. Zhoua, J. Yu, B. Chenga, H. Yu, Mater. Chem. Phys. 93 (2005) 159.
[6] M. Zhoua, J. Yu, B. Chenga, J. Hazard. Mater. B 137 (2006) 1838.
[7] C. Adán, A. Bahamonde, M. Fernández-García, A. Martínez-Arias, Appl. Catal. B 72 (2007) 11.
[8] W.-C. Hung, S.-H. Fu, J.-J. Tseng, H. Chu, T.-H. Ko, Chemosphere 66 (2007) 2142.
[9] W. Zhang, Y. Li, S. Zhu, F. Wang, Chem. Phys. Lett. 373 (2003) 333.
[10] S.-M. Oh, S.-S. Kim, J.E. Lee, T. Ishigaki, D.-W. Parka, Thin Solid Films 435 (2003) 252.
[11] A. Kumbhar, G. Chumanov, J. Nanoparticle Res. 7 (2005) 489.
[12] N. Serpone, D. Lawless, J. Disdier, J.-M. Herrmann, Langmuir 10 (1994) 643.
[13] L. Xiao, J. Zhang, Y. Cong, B. Tian, F. Chen, M. Anpo, Catal. Lett. 111 (2006) 207.
[14] J. Zhu, W. Zheng, B. He, J. Zhang, M. Anpo, J. Mol. Catal. A 216 (2004) 35.
[15] J. Zhu, F. Chen, J. Zhang, H. Chen, M. Anpo, J. Photochem. Photobiol. A 180 (2006) 196.
[16] X.H. Wang, J.-G. Li, H. Kamiyama, Y. Moriyoshi, T. Ishigaki, J. Phys. Chem. B 110 (2006) 6804.
[17] Mst.S. Nahar, K. Hasegawa, S. Kagaya, Chemosphere 65 (2006) 1976.
[18] W.Y. Teoh, R. Amal, L. Mädler, S.E. Pratsinis, Catal. Today 120 (2007) 203.
[19] X. Zhang, M. Zhou, L. Lei, Catal. Commun. 7 (2006) 427.
[20] Mst.S. Nahar, K. Hasegawa, S. Kagaya, S. Kuroda, Sci. Technol. Adv. Mater. 8 (2007) 286.
[21] J.C. Colmenares, M.A. Aramendía, A. Marinas, J.M. Marinas, F.J. Urbano, Appl. Catal. A 306 (2006) 120.
[22] J. Zhou, Y. Zhang, X.S. Zhao, A.K. Ray, Ind. Eng. Chem. Res. 45 (2006) 3503.
[23] M. Salmi, N. Tkachenko, R.-J. Lamminmäki, S. Karvinen, V. Vehmanen, H. Lemmetyinen, J. Photochem. Photobiol. A 175 (2005) 8.
[24] E. Piera, M.I. Tejedor-Tejedor, M.E. Zorn, M.A. Anderson, Appl. Catal. B 46 (2003) 671.
[25] A. Di Paola, E. García-López, S. Ikedab, G. Marcì, B. Ohtani, L. Palmisano, Catal. Today 75 (2002) 87.
[26] J.A. Navío, G. Colón, M. Trillas, J. Peral, J.J. Xavier Domènech, J. Testa, D. Padrón, M.I. Rodríguez, Litter, Appl. Catal. B 16 (1998) 187.
[27] J. Araña, O. González Díaz, J.M. Doña Rodríguez, J.A. Herrera Melián, C. Garriga i Cabo, J. Pérez Peña, J. Carmen Hidalgo, J.A. Navío-Santos, J. Mol. Catal. A 197 (2003) 157.
[28] K.T. Ranjit, B. Viswanathan, J. Photochem. Photobiol. A 108 (1997) 79.
[29] J.A. Navío, G. Colón, M. Macías, C. Real, M.I. Litter, Appl. Catal. A 177 (1999) 111.
[30] Y. Wang, H. Cheng, Y. Hao, J. Ma, W. Li, J. Mater. Sci. 34 (1999) 3721.
[31] J.A. Wang, R. Limas-Ballesteros, T. López, A. Moreno, R. Gómez, O. Novaro, X. Bokhimi, J. Phys. Chem. B 105 (2001) 9692.
[32] Z.-M. Wang, G. Yang, P. Biswas, W. Bresser, P. Boolchand, Powder Technol. 114 (2001) 197.
[33] X.H. Wang, J.-G. Li, H. Kamiyama, M. Katada, N. Ohashi, Y. Moriyoshi, T. Ishigaki, J. Am. Chem. Soc. 127 (2005) 10982.

[34] X.H. Wang, J.-G. Li, H. Kamiyama, T. Ishigaki, Thin Solid Films 506/507 (2006) 278.

[35] J.O. Carneiro, V. Teixeira, A. Portinha, L. Dupák, A. Magalhães, P. Coutinho, Vacuum 78 (2005) 37.

[36] J.H. Jho, D.H. Kim, S.-J. Kim, K. Sub Lee, J. Alloys Comp., in press, doi:10.1016/j.jallcom.2007.04.285.

[37] D.-Y. Wang, H.-C. Lin, C.-C. Yen, Thin Solid Films 515 (2006) 1047.

[38] F. Pedraza, A. Vazquez, J. Phys. Chem. Solids 60 (1999) 445.

[39] S. Cassaignon, M. Koelsch, J.-P. Jolivet, J. Phys. Chem. Solids 68 (2007) 695.

[40] K. Kakiuchi, E. Hosono, H. Imai, T. Kimura, S. Fujihara, J. Cryst. Growth 293 (2006) 541.

[41] L.J. Alemany, M.A. Bañares, E. Pardo, F. Martin, M. Galán-Fereres, J.M. Blasco, Appl. Catal. B 13 (1997) 289.

[42] J.M. Combes, A. Manceau, G. Calas, J.Y. Bottero, Geochim. Cosmochim. Acta 53 (1989) 583.

[43] D. Mardare, V. Nica, C.-M. Teodorescu, D. Macovei, Surf. Sci. 601 (2007) 4479.

[44] S. Zhu, T. Shi, W. Liu, S. Wei, Y. Xie, C. Fan, Y. Li, Physica B 396 (2007) 177.

[45] J. Yu, M. Zhou, H. Yu, Q. Zhang, Y. Yu, Mater. Chem. Phys. 95 (2006) 193.

[46] Y. Aita, M. Komatsu, S. Yin, T. Sato, J. Solid State Chem. 177 (2004) 3235.

[47] A.R. Gandhe, S.P. Naik, J.B. Fernandes, Micropor. Mesopor. Mater. 87 (2005) 103.

[48] S. Yin, K. Ihara, Y. Aita, M. Komatsu, T. Sato, J. Photochem. Photobiol. A 179 (2006) 105.